NANOTECHNOLOGY

Visible/near-infrared subdiffraction imaging reveals the stochastic nature of DNA walkers

Jing Pan, Tae-Gon Cha, Feiran Li, Haorong Chen, Nina A. Bragg, Jong Hyun Choi*

DNA walkers are designed with the structural specificity and functional diversity of oligonucleotides to actively convert chemical energy into mechanical translocation. Compared to natural protein motors, DNA walkers' small translocation distance (mostly <100 nm) and slow reaction rate (<0.1 nm s^{-1}) make single-molecule characterization of their kinetics elusive. An important indication of single-walker kinetics is the rate-limiting reactions that a particular walker design bears. We introduce an integrated super-resolved fluorescence microscopy approach that is capable of long-term imaging to investigate the stochastic behavior of DNA walkers. Subdiffraction tracking and imaging in the visible and second near-infrared spectra resolve walker structure and reaction rates. The distributions of walker kinetics are analyzed using a stochastic model to reveal reaction randomness and the rate-limiting biochemical reaction steps.

INTRODUCTION

Synthetic nanomotors and walkers are intricately designed engineering systems that draw chemical energy from the environment and convert it into mechanical motion. Their ability to actively locomote themselves in an ever-fluctuating environment makes them a promising system in a wide range of applications (*1*–*3*). A particular type of nanowalker system uses oligonucleotides to complete the mechanochemical conversion. Biochemical reactions of DNA molecules, such as hybridization, strand displacement, and catalytic cleavage, create free-energy changes that can be turned into motion (*4*). The specificity of DNA complementary base pairing can also lead to extraordinary programmability in these systems (*5*, *6*). In the past decade, investigators have proposed DNA walkers with various walking mechanisms, which typically translocate <100 nm at a speed of 0.01 to 0.1 nm s^{-1} (*1*, *4*).

Nanometric characterization of the small structures and slow kinetics of DNA walkers has been a challenging task. Most DNA walkers are studied using ensemble measurements, such as gel electrophoresis (*7*) or Förster resonance energy transfer (FRET) (*8*). Ensemble techniques provide a good measure of averaged walker kinetics but are not capable of resolving individual walker characteristics. More advanced single-molecule (SM) techniques, such as fast-scan atomic force microscopy (AFM) (*9*), SM-FRET (*10*), and single-particle tracking (SPT) (*11*, *12*), were recently demonstrated in DNA walker studies. SM-FRET can measure the kinetics and yields of a few walker steps, whereas fast-scan AFM and SPT monitor walker position continuously to probe the kinetic characteristics during processive walking. However, limited experimental precision and a lack of compatible analysis methods have restricted the potential of AFM and SPT beyond averaged kinetics.

We previously reported a DNA walker system that integrates the biochemical functionality of DNA with the optical properties of nanomaterials (*12*). The DNA walker uses chemical energies extracted from enzymatic cleavage of RNA fuel strands and walks processively along an RNA-decorated single-walled carbon nanotube (SWCNT) track. Analysis of the walker trajectory, using a semiconductor quantum dot (QD) attached to the walker as a cargo and fluorescent marker, provided data on its average reaction rate (*13*). However, stochastic chemical kinetics from single-walker behaviors have not yet been obtained. These insights will lead to a better understanding of DNA walking mechanisms and pave the road for high-performance walker designs, but it requires characterization methods with far superior spatial and temporal resolution. In recent years, several super-resolution techniques have resolved microscopic structures well below the diffraction limit. We envision that subdiffraction imaging will provide valuable insights into DNA walker systems with unprecedented details.

Here, we present such a platform capable of simultaneous visible (VIS) and second near-infrared (NIR-II) subdiffraction imaging of DNA walkers. We use the super-resolution NIR-II image of an RNA-decorated SWCNT as a one-dimensional (1D) track on which the translocation of a QD-decorated DNAzyme walker is imaged. Using these methods, we have obtained distributions of displacement and velocity and analyzed walking randomness. With the aid of a stochastic walking model, we have identified three rate-limiting intermediate reactions in a walker stepping event. These findings will facilitate the design of highly efficient molecular motors and also benefit other biomolecular reaction studies.

RESULTS AND DISCUSSION

DNA walker system

The walker system consists of a DNAzyme-decorated CdTe/CdS QD conjugated to an SWCNT track noncovalently functionalized with RNA fuel strands (Fig. 1, A and B) (*12*). The DNAzyme strand has two recognition arms (red) and an enzymatic core (green) that cleaves the RNA fuel strand at a prearranged location (pink). Its upper recognition arm is incorporated into the QD shell through the phosphorothioation of the DNA backbone for five consecutive nucleotides (nt). The heterostructured core/shell QD is obtained by epitaxial coating of CdS on the CdTe core until the desired size (d = ~3 nm) and emission wavelength (λ = ~680 nm) are achieved (fig. S1). The valence of a walker strand on QD can be controlled by varying the DNA sequence and concentration during synthesis and is maintained at 1 for monofunctionalization in this work. The NIR-II–emitting (λ = ~1050 nm) SWCNT provides a rigid track for the walker system. Length-fractionated SWCNTs with an average length of ~500 nm and a diameter of ~0.8 nm are used for self-assembly of RNA fuel strands (*14*, *15*). The molar ratio of RNA strands on an SWCNT is determined by optical absorption (*12*, *13*), which yields an interfuel spacing of approximately

School of Mechanical Engineering, Purdue University, West Lafayette, IN 47907, USA.
*Corresponding author. Email: jchoi@purdue.edu

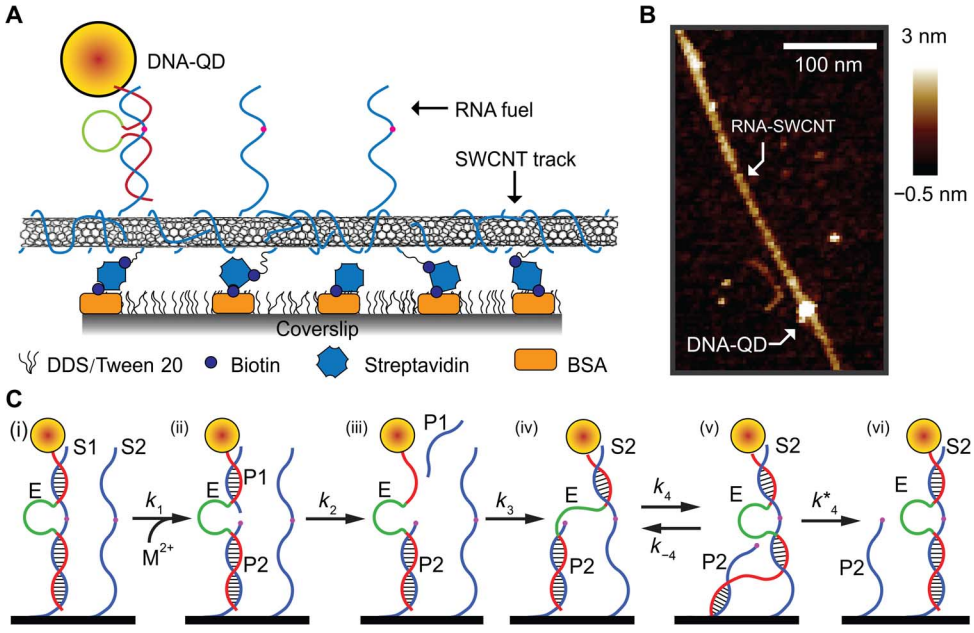

Fig. 1. DNA walker system design and walking mechanism. (**A**) Schematic of a DNA walker system on a coverslip. The coverslip surface is passivated by the combination of hydrophobic coating [dichlorodimethylsilane (DDS)] and surfactant (Tween 20). Biotinylated bovine serum albumin (biotin-BSA) is embedded into the passivation layer as an anchor point for the nanotube track. Carbon nanotubes functionalized with biotinylated RNA and RNA fuel strands bind to the surface through streptavidin/biotin interaction. The DNAzyme-decorated CdTe/CdS QD conjugates with the immobilized nanotube track through base pairing. (**B**) AFM image of a DNA-QD conjugated with an RNA-SWCNT. The striation observed along the tube axis is a result of RNA wrapping. (**C**) A single-turnover event of the enzymatic walking mechanism.

5 nm on a 500-nm-long SWCNT track (fig. S1). The detailed sequence information about both walker and fuel strands is shown in table S1.

The enzymatic reaction–based DNA walker system operates by cycling through free-energy cascades (Fig. 1C) (*4*). When a DNAzyme walker strand (E) is hybridized with a fuel strand (S1), it cleaves the RNA substrate in the presence of a divalent cation [state (i)→state (ii)], lowering the overall system free energy. The 7-nt fragment P1 then dissociates from the DNAzyme/RNA complex (EP1P2) because of thermal fluctuations [state (iii)], followed by hybridization of the upper recognition arm with the next available fuel strand S2 [state (iv)]. The lower arm then gradually migrates from P2 to S2 through strand displacement [state (iv)→state (v)] until the entire walker strand irreversibly associates with S2 [state (vi)]. This completes a single-turnover reaction (that is, one step forward). The walker repeats this process, resulting in a 1D walking along the nanotube track. It should be noted that several reaction steps are schemed as irreversible because their forward reaction rates are much faster than those of the reverse reactions (*4*, *16*). This dynamic system that directs the walker away from random diffusion by applying a biased free-energy profile is consistent with the Brownian ratchet model (*17*, *18*). Here, we use two walker strand configurations, 10–23 and DZ7 enzyme cores (*19*, *20*), with fixed 7-nt upper arm and 16-nt lower arm lengths.

VIS/NIR-II subdiffraction imaging

Nanometric optical characterization of slow-moving DNA walkers requires high-resolution imaging of both walker and track over a long period of time. We exploit the stable fluorescence from the core/shell QD and the (7,5) nanotube track to achieve high photon counts (~1000 per QD per image) with minimal photobleaching over the 1-hour experiment (fig. S2). The VIS/NIR-II emissions are imaged with a custom-built epifluorescence microscope (Fig. 2A). An electron-multiplying charge-coupled device and 2D InGaAs photodiodes are used to acquire the images from both VIS and NIR channels simultaneously. A flow-channel array is assembled using a quartz slide and a surface-passivated coverslip (fig. S3) (*21*).

The image processing schemes for both VIS and NIR channels are shown in Fig. 2B. QD images from the VIS channel are localized by fitting a 2D Gaussian function to their point spread function (PSF) [Fig. 2B, (i)]. The walker position is extracted from the centroid of the fitting. The localized QD image is then combined with the 10 successive localizations to form a single subdiffraction estimation of the QD's position [Fig. 2B, (ii)]. The localization precision on the particle position is experimentally determined to be ~20 nm (fig. S4), consistent with theoretical calculations (*22*, *23*).

The nanotube image is a concatenation of all exciton recombination centers along the tube axis. Temporal separation of these emission centers can be achieved through emission intermittency at low pH (~4) for surfactant-solubilized SWCNTs (*24*). Compared to surfactant-functionalized nanotubes, the RNA-SWCNT complexes are more susceptible to their dielectric environment as a result of the lower degree of surface coverage (*25*, *26*). We observe intensity fluctuation at pH 6 in phosphate-buffered saline (PBS) [Fig. 2B, (iv)]. The underlying intermittency spots are localized by constructing the difference image of consecutive frames and fitting the isolated PSF [Fig. 2B, (v) to (vii)]. Therefore, the combination of all the localized surface intermittency spots reconstructs a subdiffraction image of the SWCNT with ~80-nm resolution [Fig. 2B, (viii)]. The NIR and VIS images are registered to the same set of

coordinates to construct the final overlaid image shown in Fig. 2B (ix). The nanotube track images serve as markers upon which the displacements of QD cargos are visualized.

We examined DZ7 DNAzyme walking in PBS containing 20 mM dithiothreitol (DTT) and 10 mM Mg^{2+} using the optical platform. Figure 3 shows representative results of the walker traveling over 200 nm along the SWCNT track in ~10 min. The diffraction-limited raw images are shown in Fig. 3A, with red indicating the nanotube image and green representing the QD image. The displacement of the walker is shown as a 2-pixel (~127 nm per pixel) shift in the raw image. The corresponding subdiffraction images of the walker and track are shown in Fig. 3B, which clearly shows the translocation of the walker. The trajectory of the walker is plotted in Fig. 3C to demonstrate the walking distance (see movie S1 and fig. S5).

Characteristics of walker kinetics

We collected multiple 10–23 DNAzyme trajectories under the same experimental conditions. Position information from the trajectories is extracted to produce the displacement plot shown in Fig. 4A. Representative walker displacement results (blue scatter) and displacement from a control experiment (that is, 0 mM Mg^{2+}; black scatter) are shown. The positions from 10 successive frames are averaged to produce the smoothed curves (blue and black lines). The deviation from the actual data to the smoothed curve is computed for each frame to yield an average uncertainty of ~29 nm. Displacement curves from all data sets are shown in fig. S6.

Walker velocity is obtained by fitting the displacement $d(t)$ to a linear function $d(t) = \langle v \rangle t$ in a rolling time window of every 500 s. The velocity histogram is plotted in Fig. 4B and fitted to a Gaussian curve, with a mean velocity of 7.8 ± 0.37 nm min^{-1}. It should be noted that, besides processive translocations, we also observed a few cases where the walker stalled or backstepped during imaging (fig. S6B). Similar phenomena were reported previously in optical imaging of a DNA spider (*11*). Multiple factors during walker assembly and operation could interfere with the walking process, such as the stoichiometry of DNA-QD and the assembly quality of the track. We have previously demonstrated that the number of DNA walker strands per QD has a minimal impact on the walker kinetics, indicating that only one DNAzyme strand is involved in the walking process (*12*). Thus, we attribute the most likely cause for the observed stalling and backstepping to possible assembly defects on the track surface. These cases are excluded in our analysis of walker kinetics.

The directed locomotion of the walker system is confirmed by a mean squared displacement (MSD) analysis. The walker strand

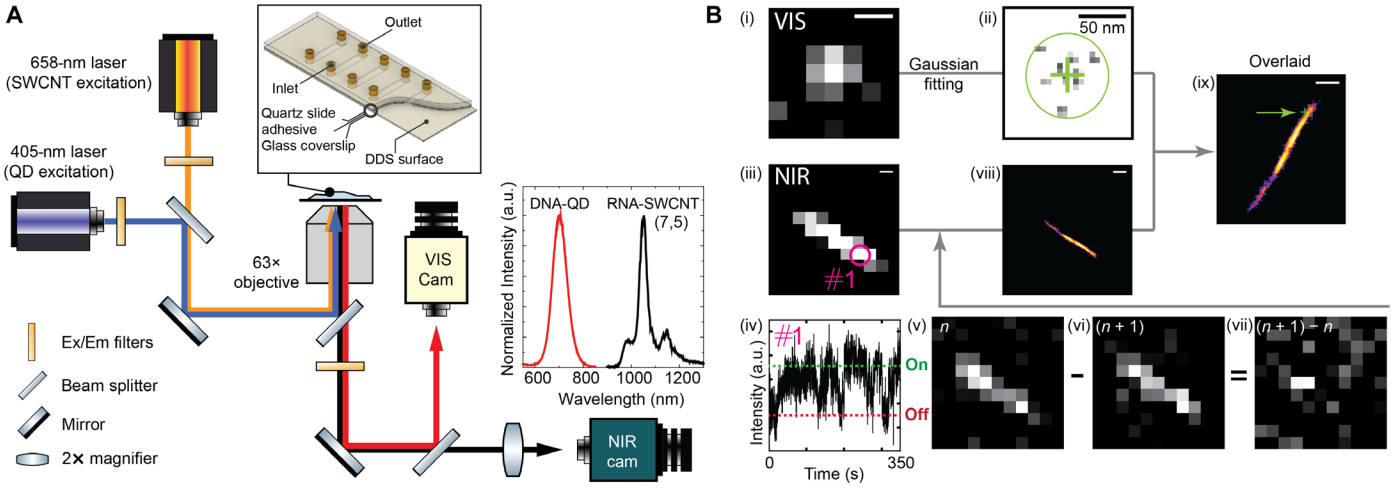

Fig. 2. Experimental setup and imaging scheme. (**A**) Excitation from two laser lines are configured as reflected light epi-illumination. Sample emissions are collected by an objective lens and separated into two light paths (VIS and NIR) for imaging with corresponding cameras. a.u., arbitrary units. (**B**) (i and ii) The PSF of a QD is fitted using a Gaussian function. The averaged localizations from 10 images form a final position estimation with ~20 nm precision. (iii and iv) Intensity fluctuation of the pixel labeled #1 in the NIR nanotube image. (v to vii) The image of isolated intensity fluctuation spot is obtained by constructing a difference image of successive frames. (viii) The isolated PSFs are localized to reconstruct the subdiffraction nanotube image. (ix) The localized VIS and NIR images are registered to the same coordinates to produce the overlaid image. The QD position is indicated by a green arrow. The scale bars are 500 nm, unless otherwise indicated.

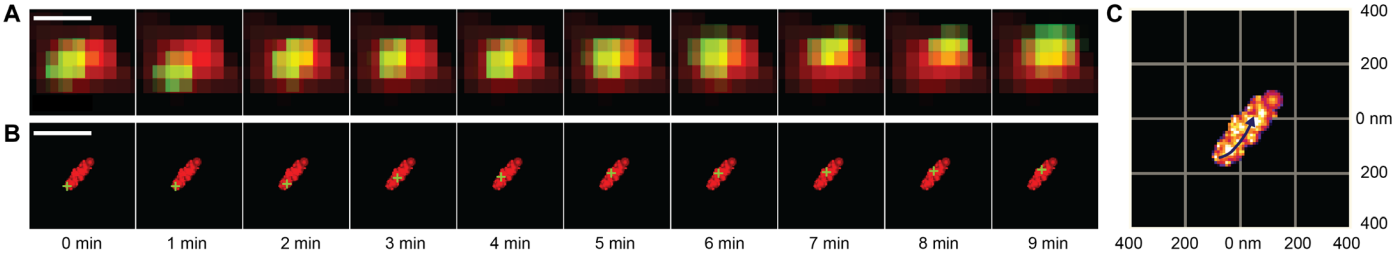

Fig. 3. Images of a DZ7 DNAzyme walker moving along an RNA-SWCNT track. (**A**) Raw and (**B**) subdiffraction images of a DZ7 DNAzyme walker in PBS containing 10 mM Mg^{2+} and 20 mM DTT. The walker travels over 200 nm in 10 min. Scale bars, 500 nm. (**C**) Walking trajectory plotted in a 400-nm × 400-nm grid for better visualization of the travel distance.

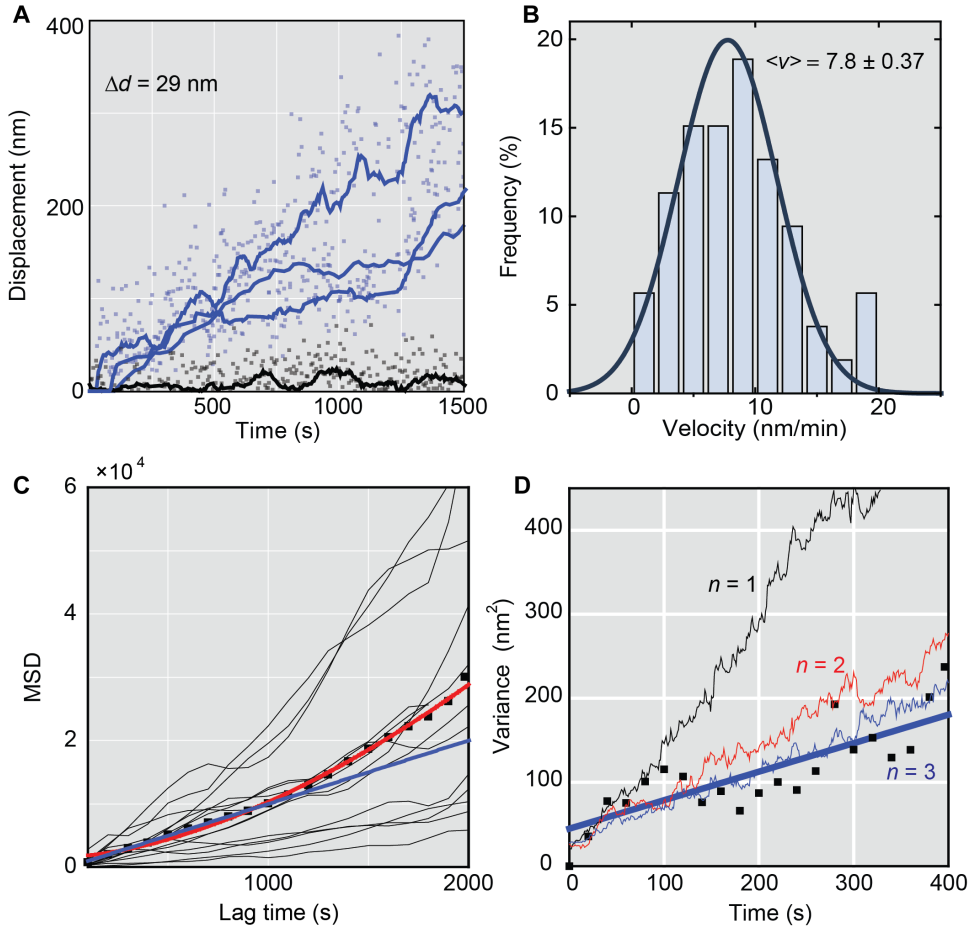

Fig. 4. Quantitative evaluation of a 10–23 DNAzyme walker. (**A**) Three representative displacements of the walker (blue scatter). The smoothed displacement from 10 successive localizations is presented in blue curves. Data from a control experiment (0 mM Mg^{2+}) are shown in black scatter and black curve. (**B**) Velocity distribution obtained from all displacement curves. Gaussian fitted histogram yields $\langle v \rangle = 7.8 \pm 0.37$ nm min^{-1}. (**C**) MSD plot of the walker. The time-averaged MSD is shown in thin black lines, and the ensemble-averaged data are plotted in black scatter. A power-law function is fitted to the experimental data with a scaling exponent of 1.7. The first 10 scatter points are linear-fitted (blue line) to better visualize the deviation of the walker MSD from diffusive motion. (**D**) Experimental and simulated mean displacement variance. The simulated results with a different number of rate-limiting steps (n) are plotted as thin curves in different colors: n = 1, black; n = 2, red; n = 3, blue. The experimental data are plotted in scatter points and linear-fitted (blue line).

forms a more stable duplex with an intact fuel strand compared to the cleaved fuel, which drives the system away from random diffusive motion to a directed translocation along the track. This Brownian ratchet–type motion can be described by a 1D biased random walk model with higher stepping probability toward the forward direction. The characteristics of this walking mechanism are reflected in the exponent of the power-law form of MSD (*27*, *28*), $\langle d(t)^2 \rangle = At^{\alpha}$. Different modes of motion can be categorized by the MSD scaling exponent α. For confined motion such as proteins crossing the cell membrane (*29*), $0 < \alpha < 1$ (subdiffusive); for random diffusion such as Brownian motion, $\alpha = 1$; for active processes such as transport by intracellular motor proteins (*30*), $1 < \alpha < 2$ (superdiffusive). Figure 4C shows the time-averaged MSD (black lines) and ensemble-averaged MSD (black scatter) constructed from the displacement plot. A power function (red line) is fitted to the experimental data, which gives $\alpha = 1.7$. A linear fitting of the first 10 scatter points (blue line) is also included to better visualize the clear curl-up shape of the walker MSD.

Fluctuation analysis

A walker system converts biochemical reactions into processive translocation, accumulating the effect of individual single-turnover events to produce a net displacement. In our DNA walker system, displacement and velocity provide a good measure of its processivity and kinetics (*13*). For example, the average single-turnover rate can be determined to be ~0.026 s^{-1} from the walker velocity (Fig. 4B). The kinetic rates associated with intermediate reactions designed in Fig. 1C may also be determined with a biophysical model (*13*). However, these model-based calculations require the walker to operate strictly as designed, whereas in the actual experiments, only the rate-limiting intermediate reactions dominate the walker behavior. Thus, identifying the number of rate-limiting biochemical reactions provides essential information about the walking mechanism and kinetics but requires insights into the stochastic behavior of a single walker.

A single-molecule enzymatic reaction is characterized by the single-turnover waiting time τ and its statistical distribution $P(\tau)$. The knowledge of this distribution helps determine kinetic intermediates in a

Table 1. Walker randomness evaluation.

Methods	Intermediate reactions	Designed *r*	Observed *r*
Simulation	1	1	1.03 ± 0.01
Simulation	2	0.5	0.49 ± 0.01
Simulation	3	0.33	0.32 ± 0.01
Stage	1	1	1.02 ± 0.12
Stage	2	0.5	0.67 ± 0.13
Stage	3	0.33	0.39 ± 0.08
DNA walker	3		0.34 ± 0.15

single-turnover reaction (*31*) or uncover the dynamic disorder of an enzyme's catalytic rate (*32*). For DNA walkers, $P(\tau)$ affects the regularity of walker stepping and, thus, is reflected in the spread of displacements from multiple walking trajectories.

We analyzed the fluctuations of walker displacement to understand the stochastic behavior of the DNA walker. Instead of using $P(\tau)$ directly, the moments of $P(N, t)$ may be used to study the fluctuation of a processive enzyme (*33*, *34*). Here, $P(N, t)$ denotes the probability of N single-turnover events that happened in time t. For processive DNAzyme walkers, the effect of single-turnover reactions accumulates to overall displacements

$$d(t) = Nl + \sigma \quad (1)$$

where l is the step length and σ is the noise term due to experimental uncertainty. At the single-molecule level, the random variable N and its statistical distribution $P(N, t)$ determine all the characteristics of the walker behavior. When there is only one rate-limiting reaction in a single-turnover event, the walker steps after an exponentially distributed dwell time [variance ($\mathrm{Var}[\tau] = 1/k^2$)] and $P(N, t)$ follow the Poisson distribution. When n rate-limiting reactions with a similar reaction rate k are present in a single turnover, the walker behaves in a less random fashion ($\mathrm{Var}[\tau] = 1/nk^2$). The second moment of $P(N, t)$ reveals this stochastic walker behavior through experimentally obtained displacement variance

$$\mathrm{Var}[d(t)] = \langle d(t)^2\rangle - \langle d(t)\rangle^2 = \frac{d(t)^2}{\tau_0}\frac{1}{n}t + \langle\sigma^2\rangle \quad (2)$$

where τ_0 is the average single-turnover time (see Materials and Methods). Equation 2 indicates that the displacement variance increases linearly with time. Its slope contains information about the number of rate-limiting reactions, whereas the intercept reflects the experimental uncertainty. Nondimensionalizing Eq. 2 gives the randomness parameter r, which is a measure of the kinetic fluctuation of the walker (*33*)

$$r = \frac{d\left(\langle d(t)^2\rangle - \langle d(t)\rangle^2\right)}{dt}\frac{2}{l\langle v\rangle} = \frac{1}{n} \quad (3)$$

The randomness parameter provides a lower-bound estimation on the number of rate-limiting steps n (*34*). The validity of this analysis method is examined by numerical simulations and controlled stage translation experiments (see the Supplementary Materials). For numerically simulated walking, a biased 1D random walk model is used with a 5-nm step length. The waiting time distribution is generated by gamma distributions with different combinations of shape (that is, number of intermediate reaction steps n) and scale (that is, reaction rate k) parameters (*31*). The mean waiting time for all cases is kept the same, so that velocity is consistent with walker experiments. Simulated displacement variance as a function of time is presented in Fig. 4D (colored thin curves) and fig. S7. For controlled stage translation experiments, the walking data generated by numerical simulations are passed to a piezo stage as translocation distance and waiting time for experimentally determining randomness. QDs tethered onto a coverslip are then imaged with the same method as walker experiments to track the stage translocation. The recovered r values from both simulations and experiments are presented in Table 1. It is evident that the analysis of the displacement variance can readily recover the designed value of r with a high precision.

We applied the fluctuation analysis to our DNA walker system to study the rate-limiting intermediate reactions during its operation. The scatter point in Fig. 4D shows experimentally obtained displacement variance, whereas the colored curves present simulated results with a different number of rate-limiting steps. A linear fitting (blue line) of the experimental data yields randomness parameter r = 0.34 and $n \approx 3$ (Table 1). This result indicates that three of the five reaction steps shown in Fig. 1C are rate-limiting. Experimentally, enzymatic cleavage (k_1), upper recognition arm dissociation (k_2), and lower arm migration (k_4) have slower reaction rates (~0.02 s^{-1}) than the hybridization of the upper arm with the next fuel strand (*12*, *13*). Thus, these three reaction steps dominate the kinetic behavior of the walker system. Tuning experimental parameters related to these reactions can significantly affect the overall system kinetics, as previously demonstrated (*13*). Furthermore, adapting more efficient reaction schemes to replace these intermediate steps could greatly enhance the walker performance. For example, nicking endonuclease or ribonuclease could significantly speed up the cleavage reaction (*35*). Using DNA origami as track could also allow one to further fine-tune system kinetic rates and randomness through a different transport mechanism (*36*).

CONCLUSIONS

The ability to identify and understand rate-limiting reactions from stochastic single-molecule kinetics will not only help formulate efficient walker mechanisms but also benefit other biomolecular reaction studies in general. In parallel, the subdiffraction imaging in the biologically transparent NIR-II window may be adapted for deep-tissue imaging and in vivo optical sensing to access more detailed structural and dynamic information about biological systems.

MATERIALS AND METHODS

Materials

All DNA and RNA sequences were custom-synthesized by Integrated DNA Technologies. The sequence information is listed in table S1. PBS containing 137 mM NaCl, 2.7 mM KCl, 1.8 mM KH_2PO_4, 10 mM Na_2HPO_4, and sodium-tris-EDTA buffer (pH 8.0; 20 mM tris-HCl,

0.5 mM EDTA, 100 mM NaCl) was prepared in deionized water (18 megohm). All reagents were purchased from Sigma-Aldrich unless noted otherwise.

Sample preparation

The RNA-coated SWCNT track and QD-decorated DNAzyme walkers were synthesized separately before performing the walking experiments. Aqueous synthesis of QD nanocrystals was previously reported by multiple groups (*37*–*40*). We modified the previously reported synthesis routes to generate DNAzyme-functionalized CdTe/CdS nanocrystal QDs. Briefly, the CdTe core with a diameter of ~2 nm was first synthesized using NaHTe and $Cd(NO_3)_2$ as precursors and mercaptopropionic acid (MPA) as capping ligand. The commercially available carboxylated CdTe core (COOH-functionalized QD; Sigma-Aldrich) can also be used for core/shell structure QD synthesis. CdS shell was grown epitaxially over the CdTe core by heating a mixture of core solution, $Cd(NO_3)_2$-MPA, and phosphorothioated DNAzyme strands at pH 12.2 for 100 min. The DNAzyme-to-CdTe core ratio was kept at 10:1 during synthesis, so that, on average, only one DNA strand was present on the QD shell layer after purification (see the Supplementary Materials). CdTe/CdS QDs with a diameter of ~3 nm and an emission peak at ~680 nm formed after heating (figs. S1A and S2). The synthesized DNA-QDs were purified using a 30,000 molecular weight cutoff (MWCO) column filtration (Amicon) for four times.

The RNA-functionalized SWCNT track was prepared by sonication with surfactants followed by dialysis with RNA for surfactant change (*12*, *41*). CoMoCAT SWCNT powder (Sigma-Aldrich) was first solubilized in 2 weight % sodium cholate (SC) and ultrasonicated at 20 W for 1 hour to obtain SC-SWCNT solution. The SC-SWCNT sample was then ultracentrifuged and thoroughly mixed with RNA fuel strands and biotin anchor strands. The RNA/SC-SWCNT mixture was then transferred to a 3000 MWCO cassette (Thermo Fisher Scientific) and dialyzed against sodium-tris-EDTA buffer for 24 hours. A second-stage 24-hour dialysis using a 100,000 MWCO membrane was carried out to remove the free, unbounded RNA strands. The RNA-SWCNT sample removed from the dialysis membrane was then centrifuged at 15,000 rpm to remove any aggregations. The length of the nanotube track was sorted to ~500 nm by adding polyethylene glycol molecules into the RNA-SWCNT sample to trigger reversible RNA-SWCNT aggregation through molecular crowding (*14*).

Experimental procedure

Coverslips and slides were thoroughly washed and passivated with dichlorodimethylsilane before performing the walking experiments (see the Supplementary Materials). In each experiment, 100 µl of biotinylated BSA solution (~0.5 mg/ml) was first introduced into the flow channel and incubated for 10 min. After BSA incubation, 100 µl of 0.2% (v/v) Tween 20 solution was introduced into the flow channel and incubated for another 10 min. We then washed out the Tween 20 solution from the channel with 100 µl of PBS buffer (pH 7.5). After washing, 100 µl of streptavidin solution (10 µg/ml) was introduced into the flow channel and incubated for 5 min. The quality of surface passivation was examined before each experiment (fig. S3).

RNA-SWCNT stock solution was diluted 10 times in PBS buffer and introduced into the flow channel. After 20 min of incubation, 200 µl of PBS buffer was introduced to wash away unbounded RNA-SWCNTs and other impurities (for example, polyethylene glycol molecules). The DNA-QD stock solution was diluted 10,000 times in PBS buffer containing 20 mM DTT. The diluted DNA-QD solution was allowed to flow continuously into the channel and imaged until sufficient conjugation spots were present. The channel was then washed with PBS buffer containing the desired concentration of metal cation and 20 mM DTT to remove unbound QDs. Both NIR and VIS images were acquired simultaneously with an integration time of 1 s. A typical experiment lasted about 1 hour, with a 20-s image acquisition interval. After each walking experiment, the PBS buffer (pH 7.5) in the channel was exchanged with a lower-pH PBS buffer (pH 6.0). The images were recorded at an integration time of 1 s for 5000 images.

Image processing

All experiment images were processed in ImageJ using custom-written scripts. Algorithms for drift correction and Gaussian fitting were adapted and modified from GDSC Single Molecule Light Microscopy (SMLM) plug-in (https://github.com/aherbert/GDSC-SMLM). Sample drift caused by mechanical relaxation of the stage was significant in DNA walking experiments as a result of the long experimental time. We used the NIR image of the nanotubes as a fiduciary marker to correct the drift in the VIS image. The (x,y) positions of RNA-SWCNTs were first approximated by finding their maxima in each frame. The subdiffraction positions of SWCNTs from 10 consecutive images were then grouped to form an image set. The drift between each image set and the average positions of all captured images were calculated using correlation analysis over the entire image. The process was repeated until convergence was achieved, and the drift from each iteration was combined to generate the final correction curve. The correction values were then applied to translate the VIS image.

The (x,y) position of the QDs was obtained by fitting their PSF to a Gaussian function. The precision σ of the fitting can be theoretically calculated by (*22*, *23*)

$$\sigma = \sqrt{\frac{s^2}{N} + \frac{a^2}{12N} + \frac{8\pi s^4 b^2}{a^2 N^2}} \quad (4)$$

where s is the standard distribution of the Gaussian distribution, a is the pixel size of the iXon3 camera, b is the background noise level, and N is the number of photons collected. Under our experimental conditions, a = 254 nm, s = 115 nm, b = ~65, and N = ~1000, which yields a localization precision σ = ~20 nm (fig. S4A).

To achieve this theoretical value from the drift-corrected image, we performed additional corrections by subtracting the displacement of stationary QDs from that of the walker-decorated QDs. The drift-corrected image was segmented into multiple areas, each containing only one QD. All the subimage areas were categorized into two groups: conjugated and nonconjugated with RNA-SWCNTs. The average position difference between frames of the nonconjugated QDs was subtracted from the position changes of the conjugated QDs. This resulted in an experimental localization precision of <30 nm, as shown in fig. S4B. The final positions of the QDs were subsequently used for the kinetic analysis.

For the super-resolution of RNA-SWCNTs, the NIR image pixel intensity fluctuation was obtained by subtracting the value from the same pixel in the successive frame. All pixel values in difference images were converted into positive integers for Gaussian fitting. According to Eq. 4, the localization precision in the NIR range is approximately 80 nm, which is about $^1/_{13}$ of the (7,5) tube emission at ~1050 nm.

Walker data analysis

The coordinates of the first 10 localizations of the QD images were averaged as the origin position (x_0,y_0) of the walker. On the basis of the average velocity, the distance traveled by the walker in this period was about 20 nm, which was within the 30-nm localization precision of our optical platform. The translocation distance $d(t)$ of the walker was calculated by computing the distance of each localization from the origin

$$d(t) = \sqrt{\left(x(t) - x_0\right)^2 + \left(y(t) - y_0\right)^2} \quad (5)$$

A rolling smoothing with a window size of 10 data points was applied to the displacement data, so that noise could be averaged out. The displacement of all the experimental cases is plotted in fig. S6. Walker velocity $\langle v\rangle = \langle d(t)\rangle/t$ was obtained by linear fitting the displacement data in every 500 s. The histogram of the velocity was approximated by a normal distribution to yield a mean velocity. The MSD was calculated by time-averaging each walker trajectory and ensemble-averaging across all trajectories

$$\mathrm{MSD} = \langle d(\delta t)^2\rangle = \frac{1}{T}\sum_{t=1}^{t=T} d(\delta t)^2 \quad (6)$$

where δt is the lag time and T is the last time point available for time average. Time-averaged MSD from different cases was ensemble-averaged to obtain the final experimental MSD value (black squares in Fig. 4C). The MSD was fitted with a power-law time dependence $\mathrm{MSD} = At^{\alpha}$. The scaling exponent $\alpha = 1.7$ was obtained from least-squares fitting.

The randomness parameter r was computed using Eq. 3, which was obtained by expanding the variance terms in Eq. 2. According to Eq. 1, the variance term in Eq. 3 can be expanded as

$$\langle d(t)^2\rangle = \langle (Nl + \sigma)^2\rangle = l^2\langle N^2\rangle + \langle \sigma^2\rangle \quad (7)$$

$$\langle d(t)\rangle^2 = l^2\langle N\rangle^2 + \langle \sigma\rangle^2 = \frac{l^2t^2}{\tau_0^2} \quad (8)$$

where $\tau_0 = n/k_i$ is the average single-turnover time, k_i is the reaction rate of an intermediate step, and $l = 5$ nm is the spacing between two neighboring fuel strands. The term $\langle N^2\rangle$ is the second moment of the distribution $P(N, t)$. When multiple intermediate steps are present in single-turnover reactions, the distribution $P(N, t)$ becomes complicated. However, the moments of $P(N, t)$ can be derived without knowing its exact distribution (*33*)

$$\langle N^2\rangle = \left(\frac{t}{\tau_0}\right)\sum_1^n \frac{\tau_i^2}{\tau_0^2} + \left(\frac{t}{\tau_0}\right)^2 \quad (9)$$

Substituting Eq. 9 into Eq. 7 yields the expression in Eq. 2, which then leads to the calculation of randomness parameter r in Eq. 3. The slope of the variance versus time plot was used for the term $d(\langle d(t)^2\rangle - \langle d(t)\rangle^2)/dt$. An interfuel spacing of $l = 5$ nm and a mean velocity of 7.8 nm min^{-1} were used.

SUPPLEMENTARY MATERIALS

Supplementary material for this article is available at http://advances.sciencemag.org/cgi/content/full/3/1/e1601600/DC1

Supplementary Methods

fig. S1. DNA-QD size distribution and RNA-SWCNT length fractionation.

fig. S2. Optical properties of DNA-QDs.

fig. S3. Imaging surface characterization.

fig. S4. Characterization of the localization and drift correction precision.

fig. S5. Images of a 10-23 DNAzyme walker moving along an RNA-SWCNT track.

fig. S6. Displacement plots of the walking experiment data sets.

fig. S7. Numerical simulations of DNA walker translocation.

table S1. Sequence information about DNA walker and RNA fuel strands.

movie S1. Raw and subdiffraction images showing a DZ7 DNAzyme walker moving along an RNA-SWCNT track.

References (*42*–*46*)

REFERENCES AND NOTES

1. J. M. Abendroth, O. S. Bushuyev, P. S. Weiss, C. J. Barrett, Controlling motion at the nanoscale: Rise of the molecular machines. *ACS Nano* **9**, 7746–7768 (2015).
2. F. Li, T.-G. Cha, J. Pan, A. Ozcelikkale, B. Han, J. H. Choi, DNA walker-regulated cancer cell growth inhibition. *ChemBioChem* **17**, 1138–1141 (2016).
3. M. von Delius, E. M. Geertsema, D. A. Leigh, A synthetic small molecule that can walk down a track. *Nat. Chem.* **2**, 96–101 (2010).
4. J. Pan, F. Li, T.-G. Cha, H. Chen, J. H. Choi, Recent progress on DNA based walkers. *Curr. Opin. Biotechnol.* **34**, 56–64 (2015).
5. P. Yin, H. M. T. Choi, C. R. Calvert, N. A. Pierce, Programming biomolecular self-assembly pathways. *Nature* **451**, 318–322 (2008).
6. R. R. F. Machinek, T. E. Ouldridge, N. E. C. Haley, J. Bath, A. J. Turberfield, Programmable energy landscapes for kinetic control of DNA strand displacement. *Nat. Commun.* **5**, 5324 (2014).
7. T. Omabegho, R. Sha, N. C. Seeman, A bipedal DNA Brownian motor with coordinated legs. *Science* **324**, 67–71 (2009).
8. I. Y. Loh, J. Cheng, S. R. Tee, A. Efremov, Z. Wang, From bistate molecular switches to self-directed track-walking nanomotors. *ACS Nano* **8**, 10293–10304 (2014).
9. S. F. J. Wickham, M. Endo, Y. Katsuda, K. Hidaka, J. Bath, H. Sugiyama, A. J. Turberfield, Direct observation of stepwise movement of a synthetic molecular transporter. *Nat. Nanotechnol.* **6**, 166–169 (2011).
10. R. Tsukanov, T. E. Tomov, M. Liber, Y. Berger, E. Nir, Developing DNA nanotechnology using single-molecule fluorescence. *Acc. Chem. Res.* **47**, 1789–1798 (2014).
11. K. Lund, A. J. Manzo, N. Dabby, N. Michelotti, A. Johnson-Buck, J. Nangreave, S. Taylor, R. Pei, M. N. Stojanovic, N. G. Walter, E. Winfree, H. Yan, Molecular robots guided by prescriptive landscapes. *Nature* **465**, 206–210 (2010).
12. T.-G. Cha, J. Pan, H. Chen, J. Salgado, X. Li, C. Mao, J. H. Choi, A synthetic DNA motor that transports nanoparticles along carbon nanotubes. *Nat. Nanotechnol.* **9**, 39–43 (2014).
13. T.-G. Cha, J. Pan, H. Chen, H. N. Robinson, X. Li, C. Mao, J. H. Choi, Design principles of DNA enzyme-based walkers: Translocation kinetics and photoregulation. *J. Am. Chem. Soc.* **137**, 9429–9437 (2015).
14. C. Y. Khripin, N. Arnold-Medabalimi, M. Zheng, Molecular-crowding-induced clustering of DNA-wrapped carbon nanotubes for facile length fractionation. *ACS Nano* **5**, 8258–8266 (2011).
15. M. J. O'Connell, S. M. Bachilo, C. B. Huffman, V. C. Moore, M. S. Strano, E. H. Haroz, K. L. Rialon, P. J. Boul, W. H. Noon, C. Kittrell, J. Ma, R. H. Hauge, R. B. Weisman, R. E. Smalley, Band gap fluorescence from individual single-walled carbon nanotubes. *Science* **297**, 593–596 (2002).
16. S. W. Santoro, G. F. Joyce, Mechanism and utility of an RNA-cleaving DNA enzyme. *Biochemistry* **37**, 13330–13342 (1998).
17. R. D. Astumian, Thermodynamics and kinetics of a Brownian motor. *Science* **276**, 917–922 (1997).
18. M. von Delius, D. A. Leigh, Walking molecules. *Chem. Soc. Rev.* **40**, 3656–3676 (2011).
19. S. W. Santoro, G. F. Joyce, A general purpose RNA-cleaving DNA enzyme. *Proc. Natl. Acad. Sci. U.S.A.* **94**, 4262–4266 (1997).
20. J. C. F. Lam, S. O. Kwan, Y. Li, Characterization of non-8–17 sequences uncovers structurally diverse RNA-cleaving deoxyribozymes. *Mol. Biosyst.* **7**, 2139–2146 (2011).
21. B. Hua, K. Y. Han, R. Zhou, H. Kim, X. Shi, S. C. Abeysirigunawardena, A. Jain, D. Singh, V. Aggarwal, S. A. Woodson, T. Ha, An improved surface passivation method for single-molecule studies. *Nat. Methods* **11**, 1233–1236 (2014).
22. H. Deschout, F. Cella Zanacchi, M. Mlodzianoski, A. Diaspro, J. Bewersdorf, S. T. Hess, K. Braeckmans, Precisely and accurately localizing single emitters in fluorescence microscopy. *Nat. Methods* **11**, 253–266 (2014).

23. A. Yildiz, P. R. Selvin, Fluorescence imaging with one nanometer accuracy: Application to molecular motors. *Acc. Chem. Res.* **38**, 574–582 (2005).
24. L. Cognet, D. A. Tsyboulski, R. B. Weisman, Subdiffraction far-field imaging of luminescent single-walled carbon nanotubes. *Nano Lett.* **8**, 749–753 (2008).
25. M. Zheng, A. Jagota, E. D. Semke, B. A. Diner, R. S. Mclean, S. R. Lustig, R. E. Richardson, N. G. Tassi, DNA-assisted dispersion and separation of carbon nanotubes. *Nat. Mater.* **2**, 338–342 (2003).
26. M. S. Strano, M. Zheng, A. Jagota, G. B. Onoa, D. A. Heller, P. W. Barone, M. L. Usrey, Understanding the nature of the DNA-assisted separation of single-walled carbon nanotubes using fluorescence and Raman spectroscopy. *Nano Lett.* **4**, 543–550 (2004).
27. N. Gal, D. Lechtman-Goldstein, D. Weihs, Particle tracking in living cells: A review of the mean square displacement method and beyond. *Rheol. Acta* **52**, 425–443 (2013).
28. M. J. Saxton, K. Jacobson, Single-particle tracking: Applications to membrane dynamics. *Annu. Rev. Biophys. Biomol. Struct.* **26**, 373–399 (1997).
29. K. Ritchie, X.-Y. Shan, J. Kondo, K. Iwasawa, T. Fujiwara, A. Kusumi, Detection of non-Brownian diffusion in the cell membrane in single molecule tracking. *Biophys. J.* **88**, 2266–2277 (2005).
30. A. Caspi, R. Granek, M. Elbaum, Enhanced diffusion in active intracellular transport. *Phys. Rev. Lett.* **85**, 5655–5658 (2000).
31. D. L. Floyd, S. C. Harrison, A. M. van Oijen, Analysis of kinetic intermediates in single-particle dwell-time distributions. *Biophys. J.* **99**, 360–366 (2010).
32. B. P. English, W. Min, A. M. van Oijen, K. T. Lee, G. Luo, H. Sun, B. J. Cherayil, S. C. Kou, X. S. Xie, Ever-fluctuating single enzyme molecules: Michaelis-Menten equation revisited. *Nat. Chem. Biol.* **2**, 87–94 (2006).
33. K. Svoboda, P. P. Mitra, S. M. Block, Fluctuation analysis of motor protein movement and single enzyme kinetics. *Proc. Natl. Acad. Sci. U.S.A.* **91**, 11782–11786 (1994).
34. M. J. Schnitzer, S. M. Block, Statistical kinetics of processive enzymes. *Cold Spring Harb. Symp. Quant. Biol.* **60**, 793–802 (1995).
35. K. Yehl, A. Mugler, S. Vivek, Y. Liu, Y. Zhang, M. Fan, E. R. Weeks, K. Salaita, High-speed DNA-based rolling motors powered by RNase H. *Nat. Nanotechnol.* **11**, 184–190 (2016).
36. E. Kopperger, T. Pirzer, F. C. Simmel, Diffusive transport of molecular cargo tethered to a DNA origami platform. *Nano Lett.* **15**, 2693–2699 (2015).
37. T.-G. Cha, B. A. Baker, J. Salgado, C. J. Bates, K. H. Chen, A. C. Chang, M. C. Akatay, J.-H. Han, M. S. Strano, J. H. Choi, Understanding oligonucleotide-templated nanocrystals: Growth mechanisms and surface properties. *ACS Nano* **6**, 8136–8143 (2012).
38. Z. Deng, A. Samanta, J. Nangreave, H. Yan, Y. Liu, Robust DNA-functionalized core/shell quantum dots with fluorescent emission spanning from UV–vis to near-IR and compatible with DNA-directed self-assembly. *J. Am. Chem. Soc.* **134**, 17424–17427 (2012).
39. N. Ma, E. H. Sargent, S. O. Kelley, One-step DNA-programmed growth of luminescent and biofunctionalized nanocrystals. *Nat. Nanotechnol.* **4**, 121–125 (2009).
40. A. Samanta, Z. Deng, Y. Liu, Aqueous synthesis of glutathione-capped CdTe/CdS/ZnS and CdTe/CdSe/ZnS core/shell/shell nanocrystal heterostructures. *Langmuir* **28**, 8205–8215 (2012).
41. J. Pan, H. Zhang, T.-G. Cha, H. Chen, J. H. Choi, Multiplexed optical detection of plasma porphyrins using DNA aptamer-functionalized carbon nanotubes. *Anal. Chem.* **85**, 8391–8396 (2013).
42. W. W. Yu, L. Qu, W. Guo, X. Peng, Experimental determination of the extinction coefficient of CdTe, CdSe, and CdS nanocrystals. *Chem. Mater.* **15**, 2854–2860 (2003).
43. X. Tu, S. Manohar, A. Jagota, M. Zheng, DNA sequence motifs for structure-specific recognition and separation of carbon nanotubes. *Nature* **460**, 250–253 (2009).
44. D. Roxbury, J. Mittal, A. Jagota, Molecular-basis of single-walled carbon nanotube recognition by single-stranded DNA. *Nano Lett.* **12**, 1464–1469 (2012).
45. A. D. Edelstein, M. A. Tsuchida, N. Amodaj, H. Pinkard, R. D. Vale, N. Stuurman, Advanced methods of microscope control using μManager software. *J. Biol. Methods* **1**, e10 (2014).
46. P. Thevenaz, U. E. Ruttimann, M. Unser, A pyramid approach to subpixel registration based on intensity. *IEEE Trans. Image Process.* **7**, 27–41 (1998).

Acknowledgments

Funding: This work was supported by the Office of Naval Research (awards N00014-15-1-2707 and N00014-12-1-0829) and the NSF (awards 1334088, 1437301, and 1512537). **Author contributions:** J.P. and J.H.C. conceived and designed the research. J.P., T-G.C., F.L., H.C., and N.A.B. performed the experiments. J.P. and J.H.C. analyzed the data. J.P. and J.H.C. wrote the manuscript with inputs from the rest of the authors. J.H.C. supervised the project. **Competing interests:** The authors declare that they have no competing interests. **Data and materials availability:** All data needed to evaluate the conclusions in the paper are present in the paper and the Supplementary Materials. Any additional data sets, analysis details, and material recipes are available upon request.

Submitted 12 July 2016
Accepted 30 November 2016
Published 20 January 2017
10.1126/sciadv.1601600

Citation: J. Pan, T.-G. Cha, F. Li, H. Chen, N. A. Bragg, J. H. Choi, Visible/near-infrared subdiffraction imaging reveals the stochastic nature of DNA walkers. *Sci. Adv.* **3**, e1601600 (2017).

Visible/near-infrared subdiffraction imaging reveals the stochastic nature of DNA walkers
Jing Pan, Tae-Gon Cha, Feiran Li, Haorong Chen, Nina A. Bragg and Jong Hyun Choi (January 20, 2017)
Sci Adv 2017, 3:.
doi: 10.1126/sciadv.1601600